nature communications

Article

https://doi.org/10.1038/s41467-024-52825-1

Upgrading of nitrate to hydrazine through cascading electrocatalytic ammonia production with controllable N-N coupling

Received: 1 April 2024

Accepted: 23 September 2024

Published online: 03 October 2024

Check for updates

Shunhan Jia[1,2], Libing Zhang[1,2], Hanle Liu[1,2,3], Ruhan Wang[1,2], Xiangyuan Jin[1,2], Limin Wu[1,2], Xinning Song[1,2], Xingxing Tan[1], Xiaodong Ma[1], Jiaqi Feng[1,4], Qinggong Zhu[1,2], Xinchen Kang[1,2], Qingli Qian[1,2], Xiaofu Sun[1,2] ✉ & Buxing Han[1,2,5] ✉

Nitrogen oxides (NO_x) play important roles in the nitrogen cycle system and serve as renewable nitrogen sources for the synthesis of value-added chemicals driven by clean electricity. However, it is challenging to achieve selective conversion of NO_x to multi-nitrogen products (e.g., N_2H_4) via precise construction of a single N-N bond. Herein, we propose a strategy for NO_x-to-N_2H_4 under ambient conditions, involving electrochemical NO_x upgrading to NH_3, followed by ketone-mediated NH_3 to N_2H_4. It can achieve an impressive overall NO_x-to-N_2H_4 selectivity of 88.7%. We elucidate mechanistic insights into the ketone-mediated N-N coupling process. Diphenyl ketone (DPK) emerges as an optimal mediator, facilitating controlled N-N coupling, owing to its steric and conjugation effects. The acetonitrile solvent stabilizes and activates key imine intermediates through hydrogen bonding. Experimental results reveal that Ph_2CN^* intermediates formed on WO_3 catalysts acted as pivotal monomers to drive controlled N-N coupling with high selectivity, facilitated by lattice-oxygen-mediated dehydrogenation. Additionally, both WO_3 catalysts and DPK mediators exhibit favorable reusability, offering promise for green N_2H_4 synthesis.

Manufacturing nitrogenous chemicals and fuels from renewable nitrogen sources using clean energy without producing harmful by-products could contribute to reduce CO_2 emissions and build our carbon-neutral and sustainable society[1–3]. Hydrazine (N_2H_4) is widely used as a reductant, anti-corrosive agent, explosives, antioxidants, and fuel for satellites and rockets[4–6]. Current industrial process for N_2H_4 production relies heavily on unsustainable chemical oxidants, including NaClO and H_2O_2 derived from pure O_2 and Cl_2 through harsh conditions (Fig. 1a). NH_3 substrates produced from energy-intensive Haber-Bosch process are used as the nitrogen source. In addition, many harmful by-products are also generated during traditional N_2H_4 production, raising notable environmental issues[7,8]. There is a pressing demand for the exploration of innovative and sustainable methods for N_2H_4 synthesis.

The excessive emission of nitrogen oxides (NO_x) poses environmental and human health concerns, but they also serve as renewable

[1]Beijing National Laboratory for Molecular Sciences, CAS Laboratory of Colloid and Interface and Thermodynamics, CAS Research/Education Center for Excellence in Molecular Sciences, Center for Carbon Neutral Chemistry, Institute of Chemistry, Chinese Academy of Sciences, 100190 Beijing, China. [2]School of Chemical Sciences, University of Chinese Academy of Sciences, 100049 Beijing, China. [3]College of Chemistry, Nankai University, 300071 Tianjin, China. [4]College of Chemical Engineering and Environment, China University of Petroleum, 102249 Beijing, China. [5]Shanghai Key Laboratory of Green Chemistry and Chemical Processes, State Key Laboratory of Petroleum Molecular & Process Engineering, School of Chemistry and Molecular Engineering, East China Normal University, 200062 Shanghai, China. ✉e-mail: sunxiaofu@iccas.ac.cn; hanbx@iccas.ac.cn

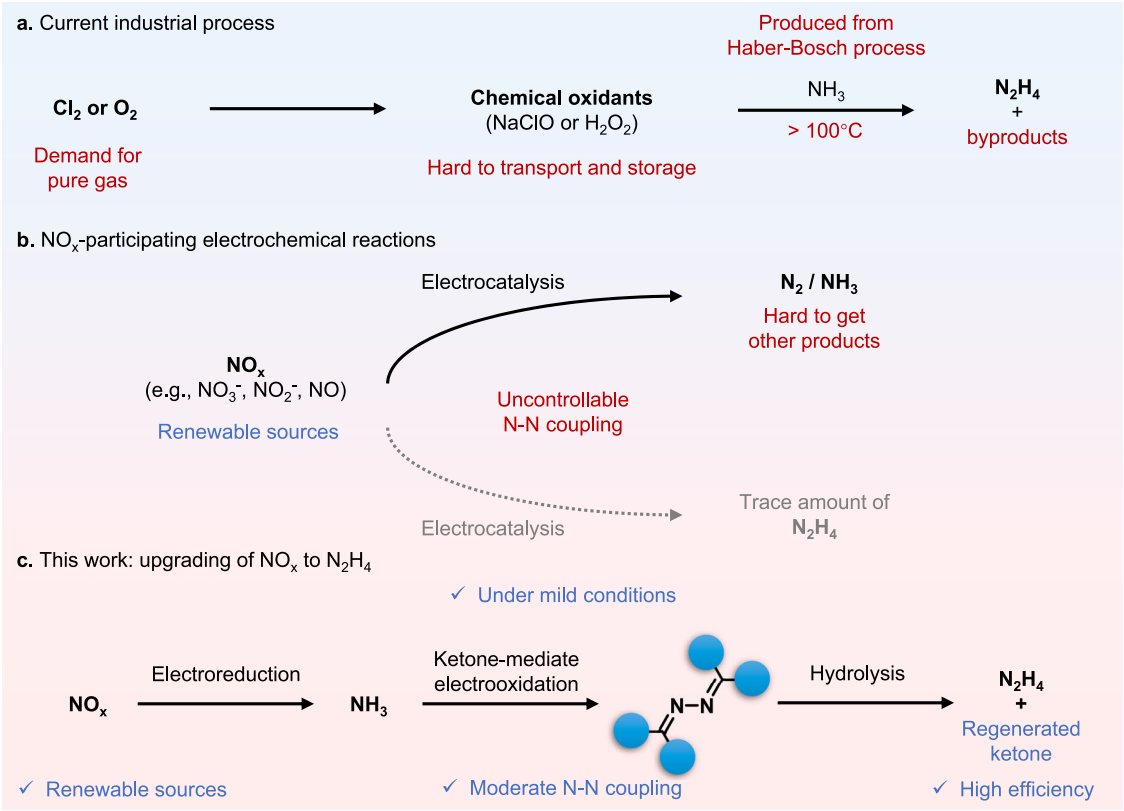

Fig. 1 | Synthesis of N_2H_4. a Schematic illustration of the traditional N_2H_4 synthesis method. **b** Recently emerging NO_x-participating electrochemical reactions. **c** Upgrading of NO_x to N_2H_4 through electrocatalysis demonstrated in this work.

nitrogen sources for the synthesis of value-added chemicals driven by clean energy[9,10]. For instance, NO_x could yield ammonia (NH_3) through electrochemical reduction (Fig. 1b)[11,12]. NO_x electroreduction is a multi-electron transfer process involving various intermediates, most of which are unstable and fleeting[13–15]. Consequently, only two thermodynamically stable products, N_2 and NH_3, are usually generated with satisfactory selectivity. Achieving selective conversion of NO_x to N_2H_4 remains a challenge, as only trace amount of N_2H_4 is detected after electrolysis due to excessive N-N coupling, leading to the formation of N_2. This excessive N-N coupling during direct NO_x reduction is attributed to the thermodynamically spontaneous nature of N-N coupling based on *NO intermediates, along with the reduction of multi-nitrogen intermediates like $*NONH_2$, $*N_2O$, and $*H_2N_2O_2$ to N_2[16,17]. Therefore, it is important to develop advanced catalytic systems to precisely control the N-N coupling, leading to the enhancement of NO_x-to-N_2H_4 efficiency.

Designing an effective catalytic system requires comprehensive consideration of pathway, solvent, and catalyst[18–20]. Various nitrogenous intermediates produced during NO_x electrolysis can either desorb directly from the catalyst surface to generate target products or couple with other intermediates[21,22]. Insufficient N-N coupling activity results in generating products with single nitrogen atom, whereas excessive N-N coupling activity leads to the formation of N≡N bonds. Hence, designing reaction pathways with mediator molecules guided by functional group protection methods in organic synthesis may be feasible. It is noteworthy that some useable nitrogenous intermediates, such as imine, are unstable in water, so it is important to choose a suitable solvent that could stabilize intermediates for controllable N-N coupling. Moreover, developing efficient heterogeneous catalysts is crucial for adsorbing intermediates and transferring charge carriers, making high reactivity and selectivity possible for N_2H_4 formation.

Herein, we report the N_2H_4 production through NO_x upgrading with controllable N-N coupling, which involves the electrochemical reduction of NO_x (with NO_3^- as an example) to NH_3, followed by ketone-mediated NH_3 oxidation for selective single N-N coupling. It was discovered that N_2H_4 was successfully synthesized with a yield of 98.5% and a Faradic efficiency (FE) of 95.6% on WO_3 catalysts. In particular, an overall selectivity of 88.7% was achieved for the conversion of NO_x to N_2H_4. Through a combination of controlled experiments, in situ characterizations, and theoretical calculations, we investigate mechanistic insights into the ketone-mediated N-N coupling process. Diphenyl ketone (DPK) was found to be the mediator for moderating N-N coupling processes owing to its unique steric and conjugate effects, which could condense with NH_3 to form imines to enable single N-N coupling. Acetonitrile (CH_3CN) solvent was used to stabilize and activate key imine intermediates through hydrogen bonding. Furthermore, we have identified the Ph_2CN^* intermediates, formed on WO_3 catalysts, as pivotal monomers driving controlled N-N coupling with high selectivity. Additionally, both the WO_3 catalyst and the DPK mediator could be reused.

Results

Upgrading of NO_3^- to N_2H_4

As illustrated in Fig. 1c, we have conducted a proof-of-concept experiment aimed at converting NO_x to N_2H_4. This was achieved through a series of steps (Supplementary Fig. S1): first, electroreduction of NO_x to NH_3; second, ketone-mediated N-N coupling of NH_3; and finally, hydrolysis of N-N products with water to yield N_2H_4. The electrocatalytic reduction of NO_x to NH_3, utilizing aqueous NO_3^- as an example, was performed using an H-type cell, employing commercial oxide-derived copper (OD Cu) as catalyst (Supplementary Fig. S2). The NH_3 product obtained from electroreduction was detected using the well-established salicylate method, as demonstrated in Supplementary

Fig. S3[23]. It should be noted that this setup is also adaptable for the reduction of other NO_x species, including NO, NO_2^-, and their mixtures[24–26]. Subsequently, the NH_3 was transferred into CH_3CN by air stripping method for further applications. The analyses revealed a high efficiency in the conversion of NO_x to NH_3, establishing NO_x-derived NH_3 as a versatile platform molecule for the synthesis of various nitrogenous chemicals.

In the following, the electrooxidation of NH_3 was carried out in a single cell with NH_3 and DPK in CH_3CN. Methanol (5 vol%) was also added to the solution as sacrificial agent, which could produce H_2 on cathode to balance the whole electrolysis cell. DPK was used as the mediator to control single N-N coupling, yielding benzophenone azine (BPA) due to its unique structure. Herein, we used WO_3/carbon paper as the working electrode due to its good ability to dehydrogenation in electrooxidation of various molecules[27–29], and the WO_3 catalyst was synthesized via a straightforward hydrothermal method employing Na_2WO_4 as the W precursor[30]. Various catalysts commonly employed in electrocatalytic oxidation reactions, such as Pt/C, Ru/C, Pd/C, MnO_2, Fe_2O_3, CoO, NiO, and CuO, were screened. Noble metal-based catalysts exhibited poor catalytic performance for the oxidation of NH_3 to BPA, with Ru/C showing no catalytic activity. In contrast, transition metal-based catalysts (MnO_2, Fe_2O_3, CoO, NiO, CuO) can catalyze the reaction, albeit with inferior performance compared to WO_3. WO_3 exhibited the highest conversion of NO_x-derived NH_3 to BPA after electrolysis, as illustrated in Supplementary Fig. S4. As a result, WO_3 was identified as the optimal catalyst for N_2H_4 synthesis because of its numerous active sites and suitable binding affinity for intermediates[31–33]. The molecular weight of 360.1 determined by gas chromatography-mass spectrometry (GC-MS) showed that the product has the molecular formula of $C_{26}H_{20}N_2$ (Supplementary Fig. S5). In addition, the selectivity of DPK-mediated N-N coupling was as high as >99.9%, since no detectable by-product was observed in GC-MS. Moreover, all the peaks in ^1H NMR and ^{13}C NMR spectra (Supplementary Fig. S5b, c) matched well with the standard samples, confirming the formation of the BPA product. Under the optimal potential of 2.1 V vs Ag/Ag^+, the FE of BPA was as high as 95.6%, with a high yield of 98.5% and selectivity of >99.9%. No detectable H_2 was produced from the surface of the anode according to GC. By employing $K^{15}NO_3$ as the reactant, we detected a molecular ion peak of the product at 362.1 (Supplementary Fig. S5e), precisely matching the calculated molecular weight of $C_{26}H_{20}{}^{15}N_2$. This finding confirmed that the nitrogen source in BPA was derived from nitrate.

Afterwards, we investigated the hydrolysis of BPA with acid aqueous solution to produce N_2H_4 (Supplementary Fig. S6). The quantification of N_2H_4 was carried out through both the colorimetric technique and ^1H NMR using standard curves in Supplementary Fig. S7[34]. According to the results from these two methods, the hydrolysis of BPA to N_2H_4 was also very efficient since the selectivity of N_2H_4 was up to 99.9%. After recrystallization of N_2H_4-based products, we could obtain $N_2H_4{\cdot}HCl$ and $(N_2H_4)_2{\cdot}H_2SO_4$ products with a yield of >60%, which exhibited similar X-ray diffraction (XRD) patterns with commercial standard samples (Supplementary Fig. S8). As a result, this tandem process exhibits remarkable efficiency, and the overall selectivity of NO_x-to-N_2H_4 was 88.7% (Supplementary Fig. S9). In contrast, direct NO_x reduction and NH_3 oxidation without the DPK mediator yielded negligible amounts of N_2H_4 after electrolysis, underscoring the necessity of designing this tandem pathway for N_2H_4 synthesis. In addition, DPK-mediated NH_3 oxidation can directly convert NH_3 to N_2H_4, offering an electrocatalytic route for N_2H_4 production compared to the traditional NH_3 oxidation pathway.

N-N coupling through lattice-oxygen-mediated dehydrogenation

The electrocatalytic N-N coupling performance using NO_x-derived NH_3 and DPK in CH_3CN solvent was evaluated through electrolysis conducted over WO_3 catalyst within a voltage range of 1.2 V to 2.2 V vs Ag/Ag^+ for 10 h (Supplementary Fig. S10). Figure 2a illustrates that the BPA selectivity remained consistently ~100% across all applied potentials. At lower potentials, the efficiency of N-N coupling was low, resulting in lower NH_3 conversion. At 2.0 V, NH_3 achieved a conversion rate to BPA as high as 98.5%, and the overall cell voltage was found to be 4.1 V. As is presented in Fig. 2b, the FE of BPA across applied potentials ranging from 1.2 V to 2.0 V consistently stands at ~95%. However, when the voltages were higher than 2.0 V, the NH_3 conversion was not notably reduced, but the FE of BPA decreased to <75% due to organic solvent molecule oxidation at high potentials. Furthermore, the WO_3 catalyst demonstrated exceptional stability, being reusable for over five cycles without notable performance decline. After being employed five times consecutively at optimal 2.0 V, the WO_3 catalyst maintained a stable current during electrolysis, achieving an NH_3 to BPA conversion rate of 99.2% and a BPA FE of 94.7% (Supplementary Fig. S11).

The evolution of intermediates during BPA formation was further studied utilizing in situ ATR-FTIR spectroscopy. The peaks at 1674 cm^{-1} (Fig. 2c), 1597 cm^{-1} (Fig. 2d), 1570 cm^{-1} (Fig. 2d), and 1450 cm^{-1} (Fig. 2e) corresponded to the H_2O produced after C-N condensation between NH_3 and DPK, the active C-N bonds in Ph_2CN^* intermediates, the DPK mediator consumed during the reaction, and the diphenyl ketone imine (DPK-I) intermediates respectively. Moreover, the observed signals of H_2O and Ph_2CN^*/DPK-I (C=N) were intensified during electrolysis, indicating an increased concentration of these intermediates in the solution, while the signal corresponding to DPK (C=O) and DPK-I (N-H) demonstrated reverse peaks, confirming its consumption. Thereinto, as DPK-I underwent N-N coupling to form BPA, the N-H signal gradually diminished. The C=N structure co-existing in both DPK-I and BPA contributed to a gradual rise in the C=N signal. As a consequence, the dehydrogenation of DPK-I generated from the condensation between NH_3 and DPK to Ph_2CN^*, followed by the dimerization of Ph_2CN^*, was essential to BPA formation, and the catalysis system should boost these steps.

The kinetics of BPA formation on the WO_3 catalyst was subsequently examined. Supplementary Fig. S12a displays the recorded yields of BPA in various reaction times conducted at the optimal electrolysis conditions, demonstrating the near-complete conversion of NH_3 into BPA after electrolysis. The rate constant k_1 of the coupling of NH_3 with DPK to form DPK-I was notably higher than the k_2 of N-N coupling between DPK-I intermediates, indicating a more favorable C-N condensation step. Consequently, the formation of BPA could be effectively approximated as a pseudo first-order reaction (Supplementary Fig. S12b), with the N-N coupling step identified as the rate-determining step (RDS). BPA was also produced by direct electrooxidation of commercial DPK-I, which also indicated that BPA was formed through N-N coupling of DPK-I intermediates. Furthermore, the findings from the linear sweep voltammetry (LSV) investigation in Supplementary Fig. S13 suggested the sluggish nature of the DPK reaction in the absence of NH_3, further supporting the preference for N-N coupling based on DPK-I intermediates.

In order to hydrolyze BPA and regenerate the BPK mediator, we dissolved the BPA product in an equivalent acid solution to generate the final N_2H_4 product. The resulting N_2H_4 product displayed a consistent unimodal peak at 3.3 ppm in ^1H NMR, aligning with the N_2H_4 standard sample, as is presented in Fig. 2f. Furthermore, the formation of N_2H_4 products was confirmed through GC-MS exhibiting a m/z of 33.00, which is the same as N_2H_4 standard and ultraviolet-visible (UV-vis) absorbance spectra (Supplementary Fig. S14). Interestingly, neither the ^1H NMR signal of N_2H_4 products nor the color development were observed in UV-vis spectra in the electrolyte obtained from direct NO_x electrocatalytic reduction. This reiterated the necessity of BPA-mediated N-N coupling processes based on NH_3 as a direct nitrogen source during N_2H_4 generation. Furthermore, the electrochemical

https://doi.org/10.1038/s41467-024-52825-1

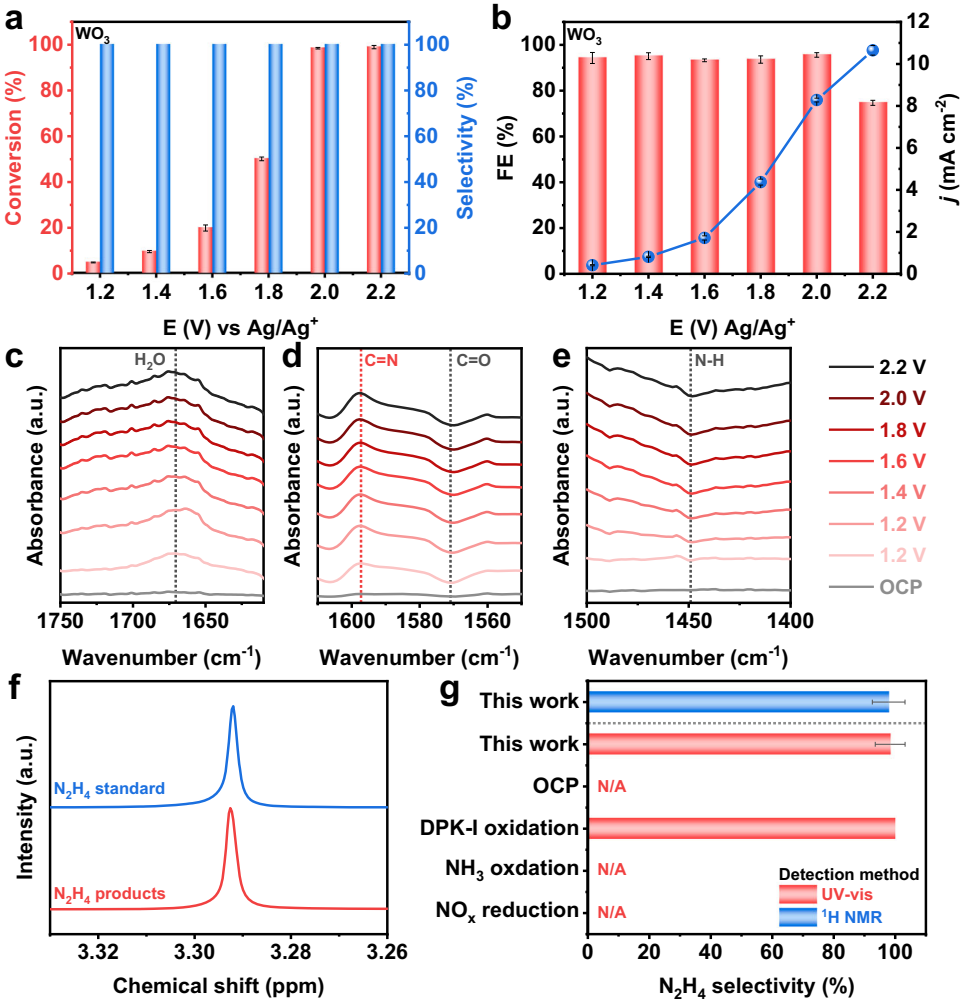

Fig. 2 | Electrochemical performance. a Conversion and selectivity of NH_3 to BPA on WO_3 catalysts under different applied potentials. **b** FE of BPA product and total current density of WO_3 catalyst under different applied potentials. ATR-FTIR spectra conducted at the surface of WO_3 catalyst under different applied potentials during BPA formation in the range of **c** 1750–1610 cm^{-1}, **d** 1610–1550 cm^{-1}, and **e** 1500–1400 cm^{-1}. **f** ^1H NMR spectra of products obtained from DPK-mediated N_2H_4 synthesis. **g** N_2H_4 yield from BPA hydrolysis detected via UV-Vis and ^1H NMR spectroscopy. All the experiments were without experiment was without iR compensation. Values are means, and error bars indicate s.d. ($n = 3$ replicates).

oxidation of DPK-I resulted in the efficient formation of Bisphenol A (BPA), thereby providing additional confirmation of the essential role played by DPK-I intermediates in BPA formation. Quantitative analysis of the N_2H_4 products, based on the integrated area of the ^1H NMR signal peak and UV-vis absorbance, revealed a very high NH_3 to N_2H_4 selectivity of >97.5%. Moreover, GC-MS, ^1H NMR, and ^{13}C NMR analyses shown in Supplementary Fig. S15 demonstrated that over 99% of the DPK could be extracted and recycled for subsequent N_2H_4 synthesis. The initial DPK feed utilized in the electrochemical reactions retained its efficacy for over 5 cycles without a considerable decrease in BPA yield. The results underscored the essentiality, efficiency, and absence of by-products in the designed reaction pathways.

XRD patterns of the WO_3 catalyst (Supplementary Fig. S16) confirmed the formation of WO_3 phase (PDF#32-1395). Scanning Electron Microscopy (SEM) (Supplementary Fig. S17) and transmission electron microscopy (TEM) (Supplementary Fig. S18) images illustrated the nanorod morphology of the obtained WO_3 electrocatalyst. High-resolution TEM (HR-TEM) images revealed consistent lattice fringes corresponding to (200) planes of WO_3 with a spacing of 0.36 nm (Fig. 3a). Energy-dispersive X-ray spectroscopy (EDS) elemental mapping (Supplementary Fig. S19) displayed a homogeneous distribution of W and O over the entire architectures. X-ray absorption near edge spectroscopy (XANES) and extended X-ray absorption fine structure (EXAFS) characterizations were carried out to get detailed structural information. The normalized W L_3-edge XANES spectra (Fig. 3b and Supplementary Fig. S20) indicated an overlap between the absorption edge of the as-prepared WO_3 catalyst and WO_3 standard sample, suggesting the presence of W^{6+} species[27,35]. As shown in Fig. 3c, Fourier transforms (FT) of the W L_3-edge EXAFS spectra suggested the presence of W-O coordination in the WO_3 electrocatalysts, with a bond length of 1.38 Å, closely resembling the WO_3 standard (1.37 Å). These findings were corroborated by X-ray photoelectron spectroscopy (XPS) (Supplementary Fig. S21). These results signify the successful synthesis of the WO_3 catalyst. More positively, the morphology and crystal structure of WO_3 catalyst did not change significantly after stability test (Supplementary Figs. S21–25). The structural features and morphology of the NiO catalyst in the control group are depicted in Supplementary Fig. S26 in the supporting information.

The coordination structure of W-O active sites in the WO_3 catalyst is crucial for overcoming the limitations of poor selectivity in the electrosynthesis of N_2H_4[34,36]. WO_3 can be rapidly and reversibly doped with hydrogen to form H_xWO_3 phase, significantly influencing reaction barriers and pathways, thereby enhancing catalytic performance[37,38]. A comparative analysis of the performance of NiO, WO_3, and W (derived

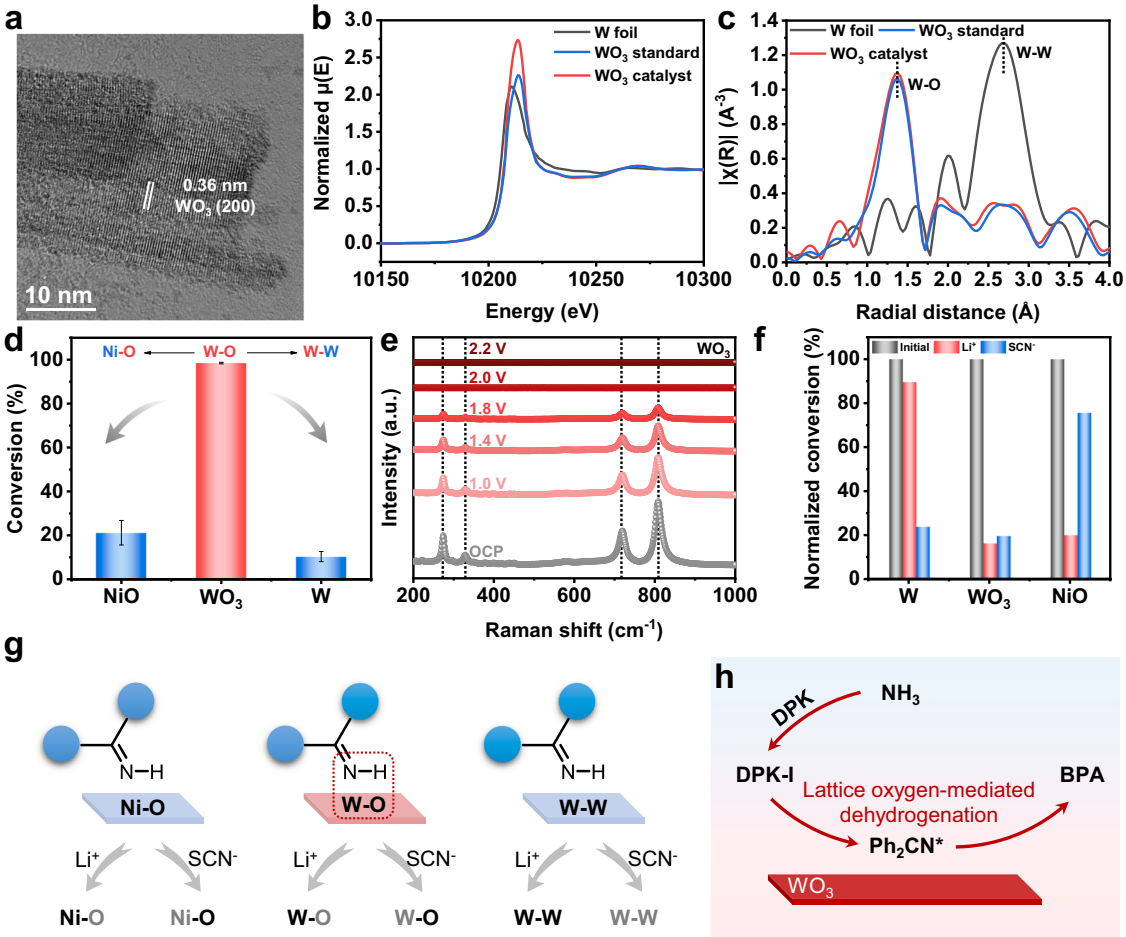

Fig. 3 | N-N coupling on WO_3 catalysts. a HR-TEM image of the WO_3 catalyst. **b** The XANES spectra of XANES spectra and **c** W L_3-edge FT EXAFS spectra of the WO_3 catalyst, along with standard samples of W foil and WO_3, highlighting W-O and W-W coordination shells. **d** Conversion of NH_3 on NiO, WO_3, and W catalyst. Values are means, and error bars indicate s.d. ($n = 3$ replicates). **e** In situ electrochemical Raman spectra over WO_3 during N_2H_4 synthesis. **f** Ratio of the NH_3 conversion on NiO, WO_3, and W catalyst before and after the poisoning experiments using Li^+ and SCN^-. **g** Illustration of the catalytic active sites during the poisoning experiments. **h** Illustration of N-N coupling on WO_3 catalyst through lattice-oxygen-mediated dehydrogenation.

from WO_3 through H_2/Ar treatment) catalysts under optimal conditions was undertaken. Despite maintaining consistent NH_3 to BPA selectivity, both the NiO and W catalysts demonstrated lower NH_3 conversion to BPA in comparison to WO_3 (Fig. 3d). This suggests that the presence of the W-O structure in the WO_3 catalyst is crucial for efficient BPA formation. The electrochemical behavior of the WO_3 catalyst was further examined through in situ Raman spectroscopy measurements. Figure 3e illustrates the characteristic peaks at 274.2 cm^{-1}, 327.9 cm^{-1}, 719.6 cm^{-1}, and 890.8 cm^{-1}, which can be associated with surface W-O bonds of WO_3[37–39]. These peaks gradually diminished with an applied potential ranging from 1.0 V to 2.0 V. This phenomenon could be attributed to the interaction of N-H bond of DPK-I with the WO_3 surface, leading to the H intercalation into the WO_3 lattice and the formation of H_xWO_3 species on the catalyst surface[40–42]. H_xWO_3, recognized as an active species present on the catalyst surface, could not drive bulk phase transitions in the WO_3 catalyst. Therefore, post-electrolysis tests verify that the structure of the used WO_3 remained comparable to its initial state. The generation of the active intermediate Ph_2CN^* from DPK-I could supply subsequent N-N coupling. In contrast, the surface of the NiO catalyst showed no noticeable active species phase with increasing potential due to the reliance of highly active NiOOH species common in electrooxidation in aqueous solution (Supplementary Fig. S27). As a result, electrooxidation reaction on NiO was not favorable due to the limited availability of H_2O in CH_3CN solvents, hindering the generation of active NiOOH site from NiO and H_2O[43–45]. DPK-I can only generate active species on the surface for N-N coupling, and no lattice species were involved. Therefore, the high electrochemical performance based on WO_3 was attributed to its ability to promote the dehydrogenation process of DPK-I under the mediation of lattice oxygen in coordination with CH_3CN solvent.

Li^+ and SCN^- poisoning experiments were conducted on WO_3, NiO, and W catalysts to elucidate the significance of the W-O lattice structure in BPA formation[38]. As illustrated in Fig. 3f, after Li^+ poisoning treatment, NiO and WO_3 catalysts experienced a substantial decrease in activity attributable to the strong coordination between Li^+ and lattice oxygen in NiO and WO_3 (Fig. 3g). Conversely, the W catalyst, lacking lattice oxygen, exhibited negligible activity decline, underscoring the role of lattice oxygen as a crucial site for BPA formation. Subsequent poisoning of the catalysts with SCN^-, known for its coordination with metal sites, revealed that WO_3 and W catalysts displayed significantly reduced performance, while NiO exhibited a comparable performance. This observation suggests the importance of W sites in the WO_3 catalyst. Consequently, the conversion from NH_3 to BPA mediated by DPK followed the NH_3→DPK-I→Ph_2CN^*→BPA pathway, with the generation of Ph_2CN^* significantly facilitated by lattice-oxygen-mediated dehydrogenation on WO_3 (Fig. 3h).

Ketone mediators to control N-N coupling

The fundamental mechanism by which ketones could facilitate single N-N coupling was illustrated in Fig. 4a, showing the stepwise

https://doi.org/10.1038/s41467-024-52825-1

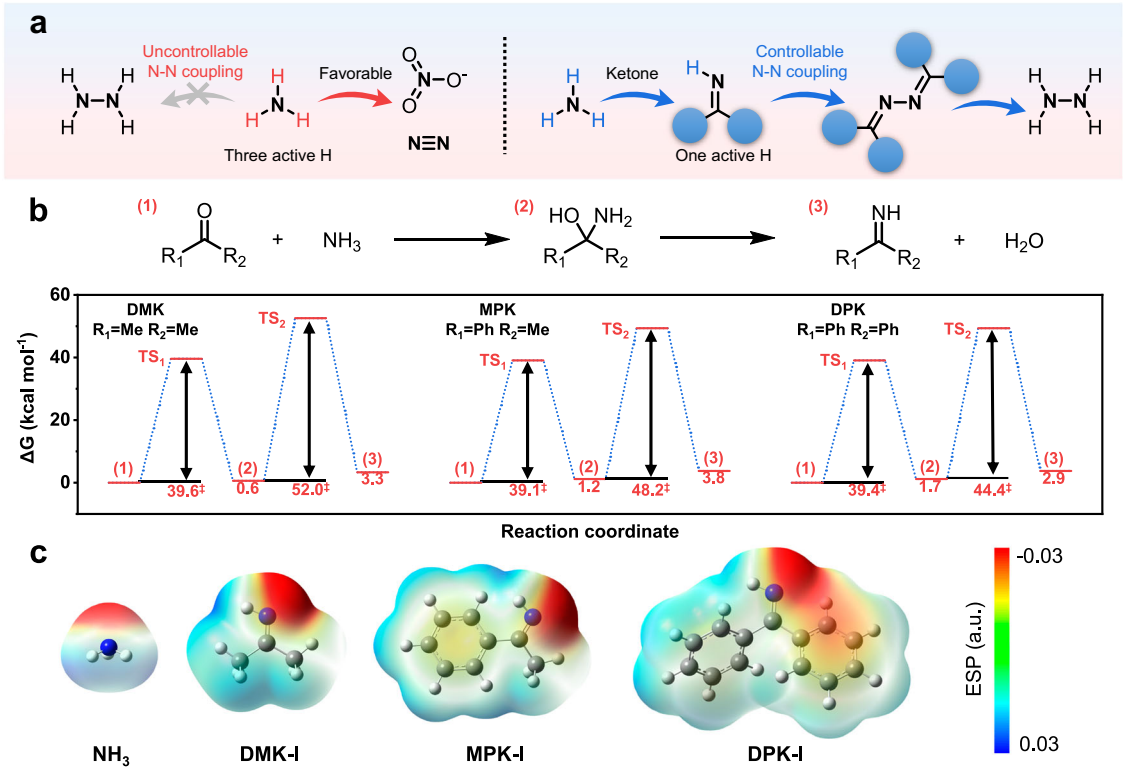

Fig. 4 | Ketone mediator. a Illustration of the molecular mechanism of ketone-mediated single N-N coupling compared with direct NH_3 oxidation. **b** Reaction pathways and calculated free energy diagrams of the condensation of DMK, MPK, and DPK with NH_3 to DMK-I, MPK-I, and DPK-I, respectively. **c** Electrostatic potentials of DMK-I, MPK-I, and DPK-I.

transformation of NH_3 to imine and ultimately N_2H_4. NH_3 molecule contains three reactive N-H bonds, and direct oxidation of these bonds results in the undesired formation of thermodynamically stable N_2 and NO_x, presenting a significant challenge in achieving exclusive N-N coupling to generate N_2H_4. Therefore, mitigating the reactivity of NH_3 becomes crucial in the pursuit of N_2H_4 synthesis. Under optimal conditions, ketones could undergo condensation with NH_3 to yield imines. N atoms could form C=N bonds, while only one C-H bond remains active within the imine molecules. Consequently, ketones may act as mediators in the controlled formation of the N-N bond, utilizing imines as a key intermediate. More importantly, C=N bonds could be simply cleaved via hydrolysis[46], providing a viable pathway for the ultimate formation of N_2H_4 through the upcycling of NO_x.

After establishing the basic methodology to produce N_2H_4, we further conducted preliminary screening of ketone compounds that could facilitate the single N-N coupling process. To investigate the influence of ketone mediator molecules with varying electronic and steric properties (Fig. 4b and Supplementary Fig. S28), we examined the energy changes involved in the condensation of three ketones with NH_3, such as dimethyl ketone (DMK), methyl phenyl ketone (MPK) and DPK. This led to the formation of imines, namely dimethyl ketone imine (DMK-I), methyl phenyl ketone imine (MPK-I), and DPK-I, following the removal of water molecules through the corresponding intermediates (supplementary data 1). The reaction transition state energy barriers from (1) to (2) for the ketones of DMK, MPK, and DPK were approximately the same, 39.6, 39.1, and 39.4 kcal mol^{-1}, respectively. However, for the reaction process from (2) to (3), the transition state energy barriers decreased gradually to 52.0, 48.2, and 44.4 kcal mol^{-1}, respectively, indicating that the activity of the DMK-I, MPK-I, and DPK-I intermediates progressively increased. Hence, DPK exhibited a higher capacity for generating DPK-I due to the boosted dehydration process, which could serve as the mediator for single N-N coupling.

Furthermore, the electrostatic potentials (φ_{max}) on the N atom side exhibited significant disparities for imines substituted with different groups: φ_{max}, DPK < φ_{max}, MPK < φ_{max}, DMK < φ_{max}, NH_3 (Fig. 4c). This discrepancy could suggest that DPK-I has the capability to redistribute the charge density on the N atom of the imine group, thereby enhancing molecular stability. This effect could be attributed to the robust conjugation of phenyl groups (Ph), which surpasses that of methyl groups (Me). Consequently, among the three selected ketone candidates, DPK emerges as a viable mediator for moderating the N-N coupling reaction in NH_3 oxidation to N_2H_4, which was achieved through the formation of DPK-I intermediates, protecting two extraneous N-H sites with imine groups of optimal stability. The superior stability of DPK-I compared to DMK-I and MPK-I was further confirmed by GC-MS analysis (Supplementary Fig. S29). This analysis revealed that only DPK-I was detectable after mixing the corresponding ketone and NH_3.

The solvent effect for DPK-I intermediates

As illustrated in Fig. 5a, the condensation of DPK and NH_3 can produce DPK-I for further N-N coupling, which demands a suitable solvent to stabilize active DPK-I intermediates. We examined the stability of DPK-I intermediates in different types of solvents, taking H_2O and CH_3CN as examples. Commercial DPK-I was mixed with each solvent in a 1:1 volume ratio and stirred for 12 h. GC-MS in Fig. 5b and Supplementary Fig. S30 analysis showed that DPK-I could be stable in CH_3CN but underwent decomposition into DPK and NH_3 in an aqueous environment. CH_3CN is a typical polar aprotic solvent and could not break the imine bonds in DPK-I intermediates, while H_2O is a highly polar solvent and participates in the hydrolysis of DPK-I to DPK and NH_3. Consequently, DPK-I intermediates were stable in CH_3CN-based non-aqueous solvents, which favors the formation of N-N bonds.

The interaction between CH_3CN and the imine functional groups in DPK-I potentially activated N-H bonds, thereby promoting N-N

https://doi.org/10.1038/s41467-024-52825-1

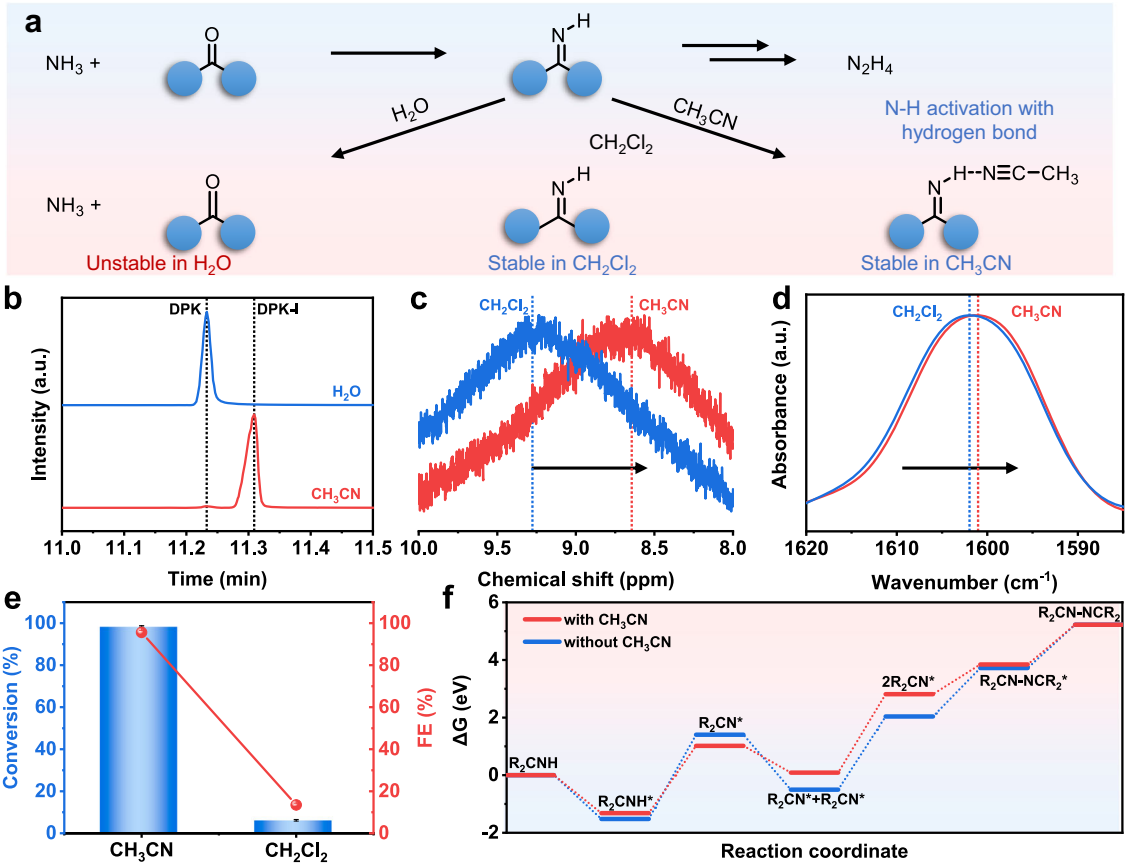

Fig. 5 | Solvent effect. a Illustration of the behavior of DPK-I intermediates in H_2O, CH_3CN, and CH_2Cl_2 solvents. **b** GC-MS curves of DPK-I treated in H_2O and CH_3CN solvents. **c** ^1H NMR spectra and **d** ATR-FTIR of DPK-I in CH_2Cl_2 and CH_3CN solvents. **e** Electrochemical performance of NH_3 to BPA transformation using CH_3CN and CH_2Cl_2 as the solvent. All the experiments were without experiment was without iR compensation. Values are means, and error bars indicate s.d. ($n = 3$ replicates). **f** Free energy of various intermediates generated during N-N coupling with and without CH_3CN.

coupling. To assess these interactions, we conducted ^1H NMR spectroscopy to analyze the DPK-I in CH_3CN and dichloromethane (CH_2Cl_2) solutions (Fig. 5c). The chemical shift of protons in the N-H groups of DKP-I exhibited shifts of 9.27 ppm to 8.63 ppm, upon dissolution in CH_2Cl_2 and CH_3CN solvents, respectively. The ^1H NMR results align with the attenuated total reflectance Fourier transform infrared (ATR-FTIR) spectra of DPK-I in diverse solvents (Fig. 5d), revealing notable shifts in peaks associated with imine groups in DPK-I. These shifts provide further evidence of hydrogen bonding formation between CH_3CN and the imine functional groups. In addition, under optimized conditions, electrochemical oxidation of NH_3 in the presence of DPK mediators was performed in CH_3CN. As depicted in Fig. 5e, the NH_3-to-BPA transformation exhibited significantly higher conversion and FE in CH_3CN than in CH_2Cl_2. Specifically, the NH_3 conversion rate was 16 times greater in CH_3CN than in CH_2Cl_2, accompanied by a corresponding 7-fold increase in FE upon transitioning from CH_2Cl_2 to CH_3CN as the solvent. As a result, while we acknowledge the intrinsic complexity of solvent systems, the existence of hydrogen bond interaction between CH_3CN and DPK-I intermediates enhances the activation of N-H bonds, facilitating the N-N coupling of DPK-I intermediates, thus promoting BPA formation.

We then investigated the reaction pathway from DPK-I to BPA with the assistance of CH_3CN molecules, utilizing a molecular model of R_2CNH ($R = CH_3$) on the surface of the $WO_3(200)$ model. The construction of the catalyst model relied on the aforementioned results concerning the characterizations of WO_3 catalysts (supplementary data 2). To simplify the calculation process, we reduced the phenyl group in DPK-I to a methyl group. Density Functional Theory (DFT) analysis shown in Fig. 5f and Supplementary Fig. S30 revealed that in the presence of CH_3CN molecules, the energy required for R_2CNH^* dehydrogenation to R_2CN^* decreased by 0.59 eV compared to the absence of CH_3CN molecules, and the Gibbs free energy for the single N-N coupling step was reduced by 0.65 eV in the presence of CH_3CN. Furthermore, the energy barrier along the reaction path with CH_3CN was generally smoother than without CH_3CN. Hence, DFT calculations could elucidate the enhanced performance of DPK-I to BPA with the assistance of CH_3CN solvent.

Discussion

In summary, we have demonstrated a strategy for green N_2H_4 synthesis by using NO_x as a renewable nitrogen source through innovative electrochemical methodology. Our approach involved electrochemical NO_x conversion to NH_3, followed by DPK-mediated NH_3 to N_2H_4 conversion, achieving an exceptional N_2H_4 yield of 98.5% with a remarkable NO_x-to-N_2H_4 selectivity of 88.7%. Detailed characterization, control experiments, and theoretical calculation revealed insights into the intricacies of controlled N-N coupling. The efficacy of DPK as a mediator in regulating N-N coupling, complemented by CH_3CN solvents stabilizing pivotal DPK-I intermediates, underscored the significance of precise mediator and solvent selection. Furthermore, Ph_2CN^* intermediates on WO_3 catalysts played a pivotal role in driving lattice-oxygen-mediated N-N coupling with high selectivity. Additionally, both WO_3 catalyst and DPK mediator demonstrated promising reusability, highlighting the potential for sustained, environmentally benign N_2H_4 synthesis. This work not only demonstrates a strategy for N_2H_4 production but also provides an in-depth understanding of the catalytic pathway. We believe that it may inspire the synthesis of other value-added chemicals that are difficult to produce by conventional routes.

Methods

Materials

Sodium tungstate dihydrate ($Na_2WO_4{\cdot}2H_2O$, 99%), tungsten trioxide (WO_3, 99.9%), potassium nitrate (KNO_3, 99.9%), benzophenone ($C_{13}H_{10}O$, 99%), potassium hexafluorophosphate (KPF_6, 99.5%), sodium salicylate ($C_7H_5NaO_3$, 99.5%), sodium hypochlorite (NaClO, active chlorine>10%), sodium nitroferricyanide dihydrate ($C_5FeN_6Na_2O{\cdot}2H_2O$, 99%), 4-(dimethylamino)benzaldehyde ($C_9H_{11}NO$, 99%), hydrazine monohydrochloride ($N_2H_4{\cdot}HCl$, 98%), hydrazinium sulfate ($N_2H_4{\cdot}H_2SO_4$, 99%), tetrabutylammonium perchlorate (TBAP, for electrochemical analysis) and nickel oxide (NiO, 50 nm) were purchased from Innochem (Beijing) Technology Co., Ltd. Copper oxide (CuO, 99.9%) was obtained from Aladdin. Ammonia (7.0 mol L^{-1} in methanol), chloroform-d ($CDCl_3$, 99.8%), deuterium oxide (D_2O, 99.8%) benzophenone imine ($C_{13}H_{11}N$, 95%), acetophenone (C_8H_8O, 99%), benzophenone imine ($C_{13}H_{11}N$, 95%), sodium 3-(trimethylsilyl) propane-1-sulfonate ($C_6H_{15}NaO_3SSi$, DSS, 99.5%) were supplied by Energy Chemicals Inc. Ammonium chloride (NH_4Cl, 99.5%), sodium sulfate (Na_2SO_4, AR), potassium sulfate (K_2SO_4, AR), hydrochloric acid (HCl, 35%), sulfuric acid (H_2SO_4, 96%), sodium hydroxide (NaOH, 99%) and were provided by Sinopharm Chemical Reagent Co., Ltd. Acetate ($C_4H_8O_2$, 99.8%), acetone (C_3H_6O, 99.8%), methanol (CH_4O, 99.9%), ethanol (C_2H_6O, 99.5%), and dichloromethane (CH_2Cl_2, 99.9%) were provided by Concord Technology (Tianjin) Co., Ltd. Toray Carbon Paper TGP-H-060 was used to load electrocatalysts. Aqueous solutions were prepared with deionized (DI) water (Millipore 18.2 MΩ cm). All the chemicals were used as received without further purification. All electrodes were supplied by Gaossunion.

Catalyst synthesis

The hydrothermal method was used to synthesize WO_3[30]. At ambient temperature, 14 mmol of $Na_2WO_4{\cdot}2H_2O$, 3.5 mmol of Na_2SO_4, and 3.5 mmol of K_2SO_4 were dissolved in 80 mL of DI water. Subsequently, the pH was adjusted to 2.0 using a 10 mol L^{-1} HCl aqueous solution until the appearance of yellow precipitates. After continuous stirring for 12 h, the solution was transferred to a Teflon-lined stainless-steel autoclave of 100 mL and subjected to heating at 180 °C for 24 h in an oven. The resulting precipitates were harvested through centrifugation, underwent repeated washing with DI water, ethanol, and acetate and were then dried under vacuum conditions at 80 °C overnight.

Electrochemical reactions

To prepare the working electrode, 10 mg of the synthesized catalyst was mixed with 1 mL of isopropanol and 20 µL of 5 wt% Nafion D-521 dispersion. After sonication for 15 min, the catalyst ink was evenly applied to 10 pieces of carbon paper (0.5 × 2 cm^2 each) using a micropipette, achieving a loading of approximately 0.5 mg cm^{-2}.

Electrochemical data were acquired using a CHI 660E electrochemical analyzer. The reduction of NO_3^- was conducted in a 1.0 mol L^{-1} KOH aqueous solution with 0.1 mol L^{-1} KNO_3 employing a typical H-cell (50 mL) separated by a Nafion 117 membrane at room temperature[21]. The Nafion 117 membrane was protonated sequentially with boiled water, 5% H_2O_2 solution, and 0.5 mol L^{-1} H_2SO_4 solution. Electrochemical reactions were performed using a three-electrode configuration, which included CuO electrocatalyst loaded on carbon paper (0.5 mg cm^{-2}) as the working electrode, an Ag/AgCl reference electrode (3 mol L^{-1} KCl solution), and a Pt film counter electrode (1 cm^2). To collect NH_3 product in CH_3CN solution for further use, NH_3 was removed from the aqueous solution to CH_3CN solution through gas stripping using Ar gas flow of 50 sccm.

Electrosynthesis of BPA was carried out in a single cell (30 mL) with a WO_3/carbon paper anode, a surface area of ~0.5 cm^2 was immersed in the solution, a platinum gauze cathode (~1.0 cm^2), and Ag/Ag^+ (0.01 mol L^{-1} $AgNO_3$ and 0.1 mol L^{-1} TBAP) reference electrode[47]. Then, 15 mL of 0.1 mol L^{-1} DPK, 0.1 mol L^{-1} NH_3 in methanol, and 0.1 mol L^{-1} KPF_6 acetonitrile solution was electrolyzed for 10 h with magnetic stirring (500 rpm). The total amount of methanol was 5 vol% of the electrolyte. Ohmic resistance (R) of the cell was 2.4 Ω, which was measured by electrochemical workstation. All the electrochemical performance tests were without experiment was without iR compensation.

In this study, the Ag/Ag^+ electrode was calibrated using ferrocene/ferrocenium (Fc/Fc^+) as the redox standard in the same solvent/electrolyte mixture as in the experiments. The Ag/AgCl electrode potential was determined using $[Fe(CN)_6]^{3-}/[Fe(CN)_6]^{4-}$ in a KCl supporting electrolyte. All the calibrations were carried out at room temperature.

Product analysis

BPA and DPK were identified using gas chromatography-mass spectrometry (GC-MS). The analysis was performed on an Agilent 5977A instrument equipped with an HP-5MS capillary column, which has a 0.25 mm internal diameter and is 30 m long. For high-resolution GC-MS, a Thermo Fisher Scientific Exactive GC system was utilized. ^1H and carbon ^{13}C nuclear magnetic resonance (NMR) spectra were recorded on a Bruker Fourier 300 spectrometer with $CDCl_3$ as the solvent.

The FE of BPA was calculated using the equation:

$$FE = \frac{nFcV}{Q} \quad (1)$$

where n represents the number of electrons transferred per mole during BPA formation, F is the Faraday constant, ccc is the concentration of the product, V is the volume of the electrolyte, and Q is the total charge passed during the reaction.

To measure the concentration of NH_3 in the catholyte, modified colorimetric techniques were employed[23]. Specifically, the salicylate method was adapted, which involved converting NH_3 to indophenol blue via a reaction with salicylate and hypochlorite. The preparation of the necessary solutions was as follows: Solution A was a mixture of 0.32 mol L^{-1} NaOH and 0.4 mol L^{-1} sodium salicylate. Solution B consisted of 0.75 mol L^{-1} NaOH mixed with sodium hypochlorite (~4.5% active chlorine). Solution C was a 10 mg mL^{-1} solution of sodium nitroprusside dihydrate. For the analysis, 3 mL of the aqueous sample was combined with 500 µL of Solution A, 50 µL of Solution B, and 50 µL of Solution C in a sample tube. A fresh electrolyte served as the blank for UV-vis measurements. A calibration curve was created by preparing standard solutions with known NH_4^+ concentrations and measuring their absorbance at 675 nm. The NH_3 concentration in the samples was determined based on this calibration curve using a Perkin Elmer Lambda 1050 + UV-vis spectrophotometer.

For the determination of N_2H_4 content, the Watt and Chrisp method was used[48]. The color reagent consisted of 5.99 g of $C_9H_{11}NO$, 30 mL of concentrated hydrochloric acid, and 300 mL of ethanol. The calibration curve was developed by preparing reference solutions with varying concentrations of hydrazine hydrate in a 0.1 mol L^{-1} hydrochloric acid solution, which was then diluted to 5 mL with deionized water. Following this, 5 mL of the color reagent was added, and the mixture was stirred for 10 min at room temperature. The absorbance was measured at 457 nm, with the hydrazine yield determined using the calibration curve established with known $N_2H_4{\cdot}HCl$ standards.

Recrystallization of N_2H_4 salts

The aqueous N_2H_4 solution was placed in a distillation flask, and the distillation apparatus was assembled. The solution was gradually heated to distill off the water, maintaining the temperature below the boiling point of hydrazine (114 °C) to prevent its loss. The concentrated hydrazine solution was then collected for further use. In a well-ventilated fume hood, concentrated HCl was added dropwise to the concentrated hydrazine solution with continuous stirring. The addition rate was carefully controlled to manage the exothermic reaction. HCl was added until the solution reached a pH of <1. The reaction

mixture was cooled in an ice bath to promote the crystallization. The mixture is left in the ice bath for 2 h to ensure complete crystallization. The hydrazine hydrochloride crystals were then isolated by vacuum filtration. The crystals were washed with a small volume of cold ethanol or acetone to remove impurities. Finally, the washed crystals were transferred to a drying oven set at 60 °C.

In situ Raman measurements

During in situ Raman measurements, a flow cell with a quartz window from GaossUnion (Tianjin) Photoelectric Technology Company was employed, utilizing the Horiba LabRAM HR Evolution Raman microscope. A 785 nm laser was utilized for excitation, and signals were captured with a 30-s integration time, averaging three scans for enhanced accuracy.

ATR-FTIR measurements

The ATR-FTIR spectra of DPK-I in different solvents were collected on a Bruker VERTEX 70 v FT-IR Spectrometer. In situ ATR-FTIR measurements were carried out in a customized electrochemical cell integrated into a Nicolet 6700 FTIR spectrometer with an MCT detector cooled by liquid nitrogen. The catalyst ink was deposited onto a germanium ATR crystal coated with a gold film. Each spectrum was acquired through 32 repetitions, maintaining a resolution of 4 cm^{-1}.

DFT calculations

All computational calculations were performed using the Gaussian16 software package[49]. The M06-2X hybrid functional was employed throughout the study[50]. Geometry optimizations were conducted with the 6-31G(d,p) basis set, and analytical frequency calculations were carried out at the same theoretical level to confirm the nature of each stationary point, identifying whether it corresponded to a minimum (characterized by no imaginary frequencies) or a transition state (indicated by a single imaginary frequency). These frequency calculations also provided Gibbs free energy corrections at 298.15 K. For the optimized structures, the final energies were refined using the larger 6-311+G(d,p) basis set.

In the case of WO_3, the computed lattice parameters were 7.309 × 7.522 × 7.678 Å, with a space group of P-1 (2). Density functional theory (DFT) calculations were carried out using the Vienna Ab initio Simulation Package (VASP). The generalized gradient approximation (GGA) was applied with the Perdew-Burke-Ernzerhof (PBE) functional. Projected augmented wave (PAW) potentials were utilized to describe the ionic cores, while the valence electrons were represented with a plane wave basis set, using a kinetic energy cutoff of 450 eV. Geometry optimizations were performed with a force convergence criterion of less than 0.05 eV $Å^{-1}$. The original bulk structures of WO_3 were optimized before surface construction, using a Monkhorst-Pack k-point grid of 5 × 5 × 5. For the WO_3(200) surface, the lattice parameter and the supercell size were set at 15.211 × 15.211 Å, with a vacuum space of 15 Å to prevent interactions between the periodic slabs. A Monkhorst-Pack k-point grid of 2 × 2 × 1 was employed for these calculations. To address the limitations of GGA, a GGA+U correction was applied, with U-J = 6.2 eV for tungsten atoms.

The Gibbs free energy change (ΔG) for each electrochemical process was calculated using the equation:

$$\Delta G = \Delta E + \Delta E_{ZPE} - T\Delta S \quad (2)$$

where ΔE represents the change in DFT energy, ΔE_{ZPE} is the zero-point energy correction, and ΔS is the entropy change at 298.15 K.

Data availability

The data that support the findings of this study are available from the corresponding author upon request. Source data are provided with this paper.

References

1. He, M., Sun, Y. & Han, B. Green carbon science: efficient carbon resource processing, utilization, and recycling towards carbon neutrality. *Angew. Chem. Int. Ed. Engl.* **61**, e202112835 (2022).
2. Jia, S. et al. Nitrogenous intermediates in NO_x-involved electrocatalytic reactions. *Angew. Chem. Int. Ed. Engl.* **63**, e202400033 (2024).
3. Jia, S. et al. In situ generation of cyclohexanone drives electrocatalytic upgrading of phenol to nylon-6 precursor. *Angew. Chem. Int. Ed. Engl.* **63**, e202410972 (2024).
4. Rees, N. V. & Compton, R. G. Carbon-free energy: a review of ammonia- and hydrazine-based electrochemical fuel cells. *Energy Environ. Sci.* **4**, 1255–1260 (2011).
5. Guo, W., Zhang, K., Liang, Z., Zou, R. & Xu, Q. Electrochemical nitrogen fixation and utilization: theories, advanced catalyst materials and system design. *Chem. Soc. Rev.* **48**, 5658–5716 (2019).
6. Zhang, T. & Asefa, T. Heteroatom-doped carbon materials for hydrazine oxidation. *Adv. Mater.* **31**, 1804394 (2019).
7. Chen, G. et al. Direct synthesis of hydrazine by efficient electrochemical ruthenium-catalysed ammonia oxidation. *Nat. Catal.* **6**, 949–958 (2023).
8. Wang, F., Gerken, J. B., Bates, D. M., Kim, Y. J. & Stahl, S. S. Electrochemical strategy for hydrazine synthesis: development and overpotential analysis of methods for oxidative N-N coupling of an ammonia surrogate. *J. Am. Chem. Soc.* **142**, 12349–12356 (2020).
9. Sharp, J. et al. Sustainable electrosynthesis of cyclohexanone oxime through nitrate reduction on a Zn-Cu alloy catalyst. *ACS Catal.* **14**, 3287–3297 (2024).
10. Udayasurian, S. R. & Li, T. Recent research progress on building C-N bonds via electrochemical NO_x reduction. *Nanoscale* **16**, 2805–2819 (2024).
11. Wu, L. et al. Efficient nitrate electroreduction over Mn-doped Cu catalyst via regulating N-containing intermediates adsorption configuration. *Sci. China Chem.* **67**, 1969–1975 (2024).
12. Zhang, Y. et al. Element-dependent effects of alkali cations on nitrate reduction to ammonia. *Sci. Bull.* **69**, 1100–1108 (2024).
13. Wu, Y. et al. Electrosynthesis of a nylon-6 precursor from cyclohexanone and nitrite under ambient conditions. *Nat. Commun.* **14**, 3057 (2023).
14. Wu, Y. et al. Electrocatalytic synthesis of nylon-6 precursor at almost 100 % yield. *Angew. Chem. Int. Ed. Engl.* **62**, e202305491 (2023).
15. Jia, S. et al. Integration of plasma and electrocatalysis to synthesize cyclohexanone oxime under ambient conditions using air as a nitrogen source. *Chem. Sci.* **14**, 13198–13204 (2023).
16. Wang, Y., Wang, C., Li, M., Yu, Y. & Zhang, B. Nitrate electroreduction: mechanism insight, in situ characterization, performance evaluation, and challenges. *Chem. Soc. Rev.* **50**, 6720–6733 (2021).
17. Xu, H., Ma, Y., Chen, J., Zhang, W.-x. & Yang, J. Electrocatalytic reduction of nitrate—a step towards a sustainable nitrogen cycle. *Chem. Soc. Rev.* **51**, 2710–2758 (2022).
18. Jia, S. et al. Synthesis of hydroxylamine via ketone-mediated nitrate electroreduction. *J. Am. Chem. Soc.* **146**, 10934–10942 (2024).
19. Cen, Z. et al. Upcycling of polyethylene to gasoline through a self-supplied hydrogen strategy in a layered self-pillared zeolite. *Nat. Chem.* **16**, 871–880 (2024).
20. Ma, X. et al. Heterophase intermetallic compounds for electrocatalytic hydrogen production at industrial-scale current densities. *J. Am. Chem. Soc.* **146**, 20594–20603 (2024).
21. Wu, L. et al. Boosting electrocatalytic nitrate-to-ammonia via tuning of N-intermediate adsorption on a Zn-Cu catalyst. *Angew. Chem. Int. Ed. Engl.* **62**, e202307952 (2023).
22. Zhao, Z. et al. Engineering vacancy and hydrophobicity of two-dimensional $TaTe_2$ for efficient and stable electrocatalytic N_2 reduction. *Innovation* **3**, 100190 (2022).

23. Wu, Y., Jiang, Z., Lin, Z., Liang, Y. & Wang, H. Direct electrosynthesis of methylamine from carbon dioxide and nitrate. *Nat. Sustain.* **4**, 725–730 (2021).
24. Ren, Y. et al. Microscopic-level insights into the mechanism of enhanced NH_3 synthesis in plasma-enabled cascade N_2 oxidation-electroreduction system. *J. Am. Chem. Soc.* **144**, 10193–10200 (2022).
25. Guo, X. et al. Aqueous electroreduction of nitric oxide to ammonia at low concentration via vacancy engineered FeOCl. *Angew. Chem. Int. Ed. Engl.* **63**, e202318792 (2024).
26. Liu, D.-X. et al. Gram-level NH_3 electrosynthesis via NO_x reduction on a Cu activated Co electrode. *Angew. Chem. Int. Ed. Engl.* **63**, e202315238 (2024).
27. Wang, L. et al. Regulating the local charge distribution of Ni active sites for the urea oxidation reaction. *Angew. Chem. Int. Ed. Engl.* **60**, 10577–10582 (2021).
28. Xiao, Y. et al. Selective photoelectrochemical oxidation of glycerol to glyceric acid on (002) facets exposed WO_3 nanosheets. *Angew. Chem. Int. Ed. Engl.* **63**, e202319685 (2024).
29. Wei, Z. et al. Steering electron-hole migration pathways using oxygen vacancies in tungsten oxides to enhance their photocatalytic oxygen evolution performance. *Angew. Chem. Int. Ed. Engl.* **60**, 8236–8242 (2021).
30. Zeng, W. et al. Hydrothermal synthesis, characterization of h-WO_3 nanowires and gas sensing of thin film sensor based on this powder. *Thin Solid Films* **584**, 294–299 (2015).
31. Zhao, S. et al. Lewis acid driving asymmetric interfacial electron distribution to stabilize active species for efficient neutral water oxidation. *Adv. Mater.* **36**, 2308925 (2024).
32. Xue, S. et al. Enriching surface-ordered defects on WO_3 for photocatalytic CO_2-to-CH_4 conversion by water. *Proc. Natl Acad. Sci. USA* **121**, e2319751121 (2024).
33. Jiang, L. et al. Mixed-phase WO_3 cocatalysts on hierarchical Si-based photocathode for efficient photoelectrochemical Li extraction. *Angew. Chem. Int. Ed. Engl.* **62**, e202304079 (2023).
34. Chen, Y. et al. Scalable decarboxylative trifluoromethylation by ion-shielding heterogeneous photoelectrocatalysis. *Science* **384**, 670–676 (2024).
35. Chen, Z. et al. Metallic W/WO_2 solid-acid catalyst boosts hydrogen evolution reaction in alkaline electrolyte. *Nat. Commun.* **14**, 5363 (2023).
36. Wang, W. et al. Enrooted-type metal-support interaction boosting oxygen evolution reaction in acidic media. *Angew. Chem. Int. Ed. Engl.* **63**, e202406947 (2024).
37. Chen, J. et al. Reversible hydrogen spillover in Ru-WO_{3-x} enhances hydrogen evolution activity in neutral pH water splitting. *Nat. Commun.* **13**, 5382 (2022).
38. Zheng, X. et al. Tailoring a local acid-like microenvironment for efficient neutral hydrogen evolution. *Nat. Commun.* **14**, 4209 (2023).
39. Xie, C. et al. In-situ phase transition of WO_3 boosting electron and hydrogen transfer for enhancing hydrogen evolution on Pt. *Nano Energy* **71**, 104653 (2020).
40. Mitchell, J. B., Lo, W. C., Genc, A., LeBeau, J. & Augustyn, V. Transition from battery to pseudocapacitor behavior via structural water in tungsten oxide. *Chem. Mater.* **29**, 3928–3937 (2017).
41. Jiang, H. et al. Insights on the proton insertion mechanism in the electrode of hexagonal tungsten oxide hydrate. *J. Am. Chem. Soc.* **140**, 11556–11559 (2018).
42. Cui, Y. et al. Discoloration effect and one-step synthesis of hydrogen tungsten and molybdenum bronze (H_xMO_3) using liquid metal at room temperature. *ACS Omega* **4**, 7428–7435 (2019).
43. Zhou, B. et al. Platinum modulates redox properties and 5-hydroxymethylfurfural adsorption kinetics of $Ni(OH)_2$ for biomass upgrading. *Angew. Chem. Int. Ed. Engl.* **60**, 22908–22914 (2021).
44. Chen, W. et al. Vacancy-induced catalytic mechanism for alcohol electrooxidation on nickel-based electrocatalyst. *Angew. Chem. Int. Ed. Engl.* **63**, e202316449 (2024).
45. Feng, F. et al. Breaking highly ordered PtPbBi intermetallic with disordered amorphous phase for boosting electrocatalytic hydrogen evolution and alcohol oxidation. *Angew. Chem. Int. Ed. Engl.* **63**, e202405173 (2024).
46. Lan, X. et al. Electrosynthesis of hydroxylamine from nitrate reduction in water. *Sci. China Chem.* **66**, 1758–1762 (2023).
47. Song, X. et al. Boosting CO_2 electroreduction over Co nanoparticles supported on N,B-co-doped graphitic carbon. *Green Chem.* **24**, 1488–1493 (2022).
48. Lv, C. et al. A defect engineered electrocatalyst that promotes high-efficiency urea synthesis under ambient conditions. *ACS Nano* **16**, 8213–8222 (2022).
49. Frisch, M. J. et al. Gaussian 16, Rev. C.01 (Gaussian, Inc., 2016).
50. Zhao, Y. & Truhlar, D. G. The M06 suite of density functionals for main group thermochemistry, thermochemical kinetics, noncovalent interactions, excited states, and transition elements: two new functionals and systematic testing of four M06-class functionals and 12 other functionals. *Theor. Chem. Acc.* **120**, 215–241 (2008).

Acknowledgements

The work was supported by the National Natural Science Foundation of China (22293015 and 22121002), the Strategic Priority Research Program (A) of the Chinese Academy of Sciences (XDA0390400), the CAS Project for Young Scientists in Basic Research (Grant No. YSBR-050), and the Photon Science Center for Carbon Neutrality. The X-ray absorption spectroscopy measurements were performed at Beamline 1W1B at the Beijing Synchrotron Radiation Facility (BSRF). The authors thank the staff at the Centre for Physiochemical Analysis & Measurement of ICCAS for material characterizations.

Author contributions

S.H.J., X.F.S., and B.X.H. proposed the project, designed the experiments, and wrote the manuscript; S.H.J. performed the whole experiments; L.B.Z., H.L.L., R.H.W., X.Y.J., L.M.W., X.N.S., X.X.T., X.D.M., and J.Q.F. conducted a part of characterizations. Q.G.Z., X.C.K., and Q.L.Q. participated in discussions. X.F.S. and B.X.H. supervised the whole project.

Competing interests

The authors declare no competing interests.

Additional information

Supplementary information The online version contains supplementary material available at https://doi.org/10.1038/s41467-024-52825-1.

Correspondence and requests for materials should be addressed to Xiaofu Sun or Buxing Han.

Peer review information *Nature Communications* thanks Tengfei Li and the other anonymous reviewer(s) for their contribution to the peer review of this work. A peer review file is available.